Inverse Opal-Like, Ca3Al2O6-Stabilized, CaO-Based CO2 Sorbent: Stabilization of a Highly Porous Structure To Improve Its Cyclic CO2 Uptake

Author(s):
Kim, Sung Min; Armutlulu, Andac; Kierzkowska, Agnieszka M.; Müller, Christoph R.

Publication date:
2019-09-23

Permanent link:
https://doi.org/10.3929/ethz-b-000366080

Originally published in:
ACS Applied Energy Materials 2(9), https://doi.org/10.1021/acsaem.9b01058

Funding acknowledgement:
156015 - Next generation CaO-based CO2 sorbents: X-ray absorption spectroscopy and advanced electron microscopy techniques (SNF)

Inverse opal-like, $Ca_3Al_2O_6$-stabilized, CaO-based CO_2 sorbent: stabilization of a highly porous structure to improve the cyclic CO_2 uptake

Sung Min Kim, Andac Armutlulu, Agnieszka M. Kierzkowska, and Christoph R. Müller*

Department of Mechanical and Process Engineering, ETH Zurich, Leonhardstrasse 21, 8092 Zurich, Switzerland

KEYWORDS: Inverse opal-like structure, hierarchical porosity, carbon sphere template, calcium oxide, $Ca_3Al_2O_6$ stabilizer, CO_2 capture

ABSTRACT: Effective CO_2 sorbents were manufactured utilizing inverse opal (IO)-like, CaO-based structures enabled by carbon nanosphere templates. To stabilize the structures against sintering, $Ca_3Al_2O_6$ was incorporated via three different routes, i.e., one-pot synthesis, impregnation and atomic layer deposition (ALD). The sorbents realized through one-pot and ALD-assisted synthesis methods exhibited a significantly enhanced CO_2 uptake when compared to the benchmark limestone and the sorbent realized by post-synthesis impregnation. The differences in the performance of the materials were rationalized by relating the textural properties of the material to the CO_2 uptake in the kinetically- and diffusion-limited carbonation stages. We observe, that both the kinetically and diffusion-limited carbonation stages are critically linked to the volume in pores with $d_{pore} < 100$ nm and the surface area of the material.

1. INTRODUCTION

CO_2 is a major greenhouse gas contributing significantly to global warming[1-2]. According to the International Energy Agency (IEA)[3] anthropogenic CO_2 emissions have reached 32 Gt in 2014 and are foreseen to increase to 57 Gt in 2050.[4] To fulfil the ambitious aim to limit the increase in the average global temperature to 2 °C, anthropogenic greenhouse gas emissions have to be reduced significantly.[3] In this context, carbon dioxide capture and storage (CCS) is considered as a near- to mid-term solution with a potential to reduce CO_2 emissions by 8.2 Gt/yr by 2050.[5] An alternative, is the subsequent conversion of the CO_2 captured into chemicals and/or fuels (as opposed to underground storage).[6-11] For example, CO_2 capture and utilization (CCU) can offer new pathways to convert the CO_2 captured in the sorbent regeneration step e.g. through the direct integration of the dry reforming of methane (DRM) into calcium looping leading to potential energy savings.[12]

So far, amine scrubbing is the most advanced technology for the removal of CO_2 from a gas stream.[5] However, monoethanolamine (MEA)-based sorbents suffer from thermal degradation. In addition, their reaction with flue gas impurities, such as SO_2, NO_2 and O_2,[13-14] can lead to the formation of toxic substances, e.g., nitrosamines [15-16]. Hence, the development of less costly and environmentally more benign CO_2 capture sorbents is actively pursued to enable the large-scale implementation of CCS. In this regard, solid CO_2 sorbents such as alkaline earth metal oxides, metal hydroxides,[17] layered double oxides (LDO),[18] activated carbon,[19-20] or metal organic frameworks (MOF)[21-22] have shown promising CO_2 capture characteristics. Among these materials, CaO stands out due to high abundance of natural precursors (e.g., limestone and dolomite), high theoretical CO_2 capture capacity (0.78 g CO_2/g sorbent), and fast CO_2 capture. The CO_2 capture process relying on CaO as a sorbent, commonly referred to as calcium looping (CaL), proceeds via the following reversible reaction:

$$CaO + CO_2 \leftrightarrows CaCO_3,\ \Delta H^0_{298K} = \pm 178\ kJ/mol$$

The CO_2 capture costs of CaL have been estimated to be in the range of 12–32 € per ton of CO_2 captured,[23-24] which is considerably lower compared to conventional amine scrubbing (34–67 €/t CO_2), pressure swing adsorption (26–33 €/t CO_2) or membrane separation (31–36 €/t CO_2).[24]

However, CaO derived from naturally occurring precursors, e.g., limestone shows a rapid decay in its ability to reversibly capture and release CO_2. This performance decay of the sorbent has been attributed to the sintering of the material, as the Tammann temperature of $CaCO_3$ (≈ 533 °C) is appreciably below the operating temperature of the process (650–900 °C). Sintering leads to irreversible and detrimental changes in the textural properties of the sorbent (notably its surface area and pore volume)[25-26], which play a crucial role in the CO_2 uptake capacity of the sorbent, owing to the large volumetric expansion of the sorbent upon CO_2 capture (the ratio of the molar volume of $CaCO_3$ to CaO is 2.2).

To minimize the detrimental effects of sintering, the stabilization of CaO through the incorporation of high-Tammann-temperature metal oxides, e.g., Al_2O_3, MgO, TiO_2, SiO_2, MnO_2 and ZrO_2 [27-37], has been proposed. Besides the total CO_2 uptake capacity, also the rate of CO_2 capture is an important characteristic owing to limited residence times in industrial reactors (e.g. circulating fluidized beds). The carbonation of CaO typically proceeds in two successive steps.[38-39] In the first step, carbonation proceeds rapidly in a kinetically controlled regime. With a growing thickness of the product layer of $CaCO_3$, the reaction transitions to a sluggish diffusion-limited regime (the diffusivity of CO_2 through $CaCO_3$, $D_{CaCO3} = 0.003$ cm^2/s, is two orders of magnitude smaller compared to CaO, $D_{CaO} = 0.3$ cm^2/s). The critical product layer, at which this transition occurs has been

estimated as 50 nm.[38] Hence, to ensure a high CO_2 uptake in the kinetically controlled regime a sorbent has to feature two essential morphological characteristics: (i) nano-structuring to minimize diffusion lengths of CO_2 through the $CaCO_3$ product layer, and (ii) high porosity to allow for the rapid diffusion of CO_2 and to compensate for the large volumetric expansion upon carbonation.

Various synthesis techniques, including wet-mixing [40], co-precipitation [41], hydration [42], thermal pre-treatment [43], flame spray pyrolysis [30, 44], hydrolysis [25] and sol-gel [28, 45-46] have been employed to introduce a stabilizer, e.g., $Ca_{12}Al_{14}O_{33}$,[47] $Ca_3Al_2O_6$,[32, 48] $CaZrO_3$[49] and MgO[50] into the CaO matrix. However, all of these techniques have their short-comings when it comes to yielding a material that features both a desirable nano-structured morphology and compositional homogeneity. Recently, sacrificial templates have been employed as a means to obtain inverse opal (IO)-like structures of $CaCO_3$ or CaO. Some of these materials also contained structural stabilizers, e.g., MgO, ZrO_2, Al_2O_3 and Y_2O_3, to alleviate a sintering-induced capacity decay of the CO_2 sorbents.[51] More recently, atomic layer deposition (ALD) has been explored as a means to deposit a structural stabilizer, e.g., Al_2O_3, onto a $CaCO_3$ structure in a very controlled fashion as it allows for thickness control at the atom level.[32] However, we currently do not have an in-depth understanding on how to optimize the structure, location and quantity of a stabilizer to maximize the stability of the textural properties of a sorbent and in turn its CO_2 uptake.

Herein, we have synthesized an IO-like, CaO-based structure using biomass-derived carbon nanospheres (CNS) as a sacrificial template. A structural stabilizer was introduced into the IO-like structure using different approaches, i.e., directly during synthesis, via conventional impregnation or by ALD. The CO_2 uptake along with the textural and morphological characteristics of the materials were scrutinized in detail, allowing us to correlate the CO_2 uptake with structural and morphological features.

2. EXPERIMENTAL SECTION

2.1. Materials. Calcium nitrate tetrahydrate (Acros, 99%), aluminium nitrate nonahydrate (Acros, ≥ 99%), trimethyl aluminum (TMA, Pegasus Chemicals, electronic grade), D-(+)-glucose (Sigma-Aldrich, ≥ 99.5%), and boric acid (Fisher, laboratory reagent grade) were purchased and used without further purification.

2.2. Preparation of carbon nanosphere (CNS). CNS were prepared via the carbonization of D-(+)-glucose under hydrothermal conditions using the protocol proposed by Sun *et al.* [52]. Briefly, an aqueous solution of glucose with various concentrations (0.6, 1.1 M and 2.2 M) was transferred into a teflon-lined stainless steel autoclave. The hydrothermal treatment was carried out at 180 °C for 12 h. The resulting material was collected, washed with deionized water and anhydrous ethanol, alternatingly five times, and dried at 80 °C overnight in an oven. The particle size of the as-synthesized CNS was determined by HR-SEM, and the obtained spheres are denoted as CNS (particle size).

2.3. Preparation of IO-like, $Ca_3Al_2O_6$-stabilized, CaO-based CO_2 sorbents. The sorbents were prepared by incipient wetness impregnation using the CNS template (1.5 g and BJH pore volume of 0.32 cm^3/g) and a 10 M aqueous solution (0.3 ml) of calcium nitrate and aluminium nitrate (depending on the material the molar ratio of calcium to aluminium ranged from 10:0 to 0:10). The samples were dried in a vial at room temperature for 1 day to avoid melting of the nitrates. The resulting material was carburized at 500 °C (2 °C/min ramping rate) for 2 h in a horizontal furnace in a N_2 flow of 0.4 L/min. The final sorbent was obtained after calcination at 900 °C for 2 h (5 °C/min) in a muffle furnace. The sorbents obtained are abbreviated as IO-Ca_xAl_y_(CNS particle size), where x and y specify the molar ratio of Ca^{2+} and Al^{3+}, respectively. An elemental analysis of the calcined materials was performed via ICP-OES (Agilent 5100 VDVV).

2.4. Deposition of an Al_2O_3 layer by ALD onto unstabilized IO-Ca_900 nm. An Al_2O_3 overcoat was deposited onto IO-Ca_900 nm using a commercial ALD reactor (Picosun R-200) equipped with a system for the coating of powders. TMA and de-ionized (DI) H_2O were used as the ALD precursor and oxidant, respectively, and high-purity N_2 served as both the carrier and purge gas. The pulse and purge times were kept constant at 0.1s / 15s / 0.1s / 15s for TMA / N_2 / H_2O / N_2 using three pulses for both TMA and H_2O per ALD cycle. The deposition took place at 300 °C, and the temperature of the precursors was 20 °C. A reference material was prepared by the wet-impregnation of IO-Ca_900 nm in an aqueous solution of aluminium nitrate. Specifically, 50 mg of IO-Ca_900 nm was added to an aqueous solution (100 ml) containing 21 mg of aluminium nitrate (1.0 M). After stirring for 5 h, the water was evaporated in a rotary evaporator (Heidoph) at 80 °C (300 mbar) and dried further at 100 °C overnight in an oven. Materials synthesized by ALD (20 cycles) and impregnation were calcined in a muffle furnace at 900 °C for 2 h (5 °C/min). The molar ratio of Ca^{2+} : Al^{3+} for both sorbents was 9:1, as determined by elemental analysis (ICP-OES). The ALD-based and reference material are denoted as ALD-IO-Ca_9Al_1_900 nm and IMP-IO-Ca_9Al_1_900 nm, respectively.

2.5. Characterization. Elemental analysis of the calcined materials was performed by ICP-OES (Agilent 5100 VDVV).

Fourier transform infrared (FTIR) spectra of the dried CNS was recorded with a Nicolet iS10 infra-red spectrophotometer (Thermo Scientific) equipped with a smart orbit (diamond) ATR accessory (4.8 cm^{-1} resolution).

The surface charge of the CNS was determined by zeta potential measurements (Malvern Zetasizer Nano ZS; field strength of 15 V/cm). The Zetasizer Nano measures the electrophoretic mobility of the particles in deionized water, which was converted into a zeta potential using the Smoluchowski equation.

N_2 physisorption onto the calcined and cycled sorbents were determined using a NOVA 4000e analyzer (Quantachrome In-

struments). The adsorption and desorption of N_2 was determined at -196 °C after degassing each sample (~ 50 mg) at 300 °C under vacuum for at least 3 h. The specific surface area and pore size distribution was calculated using the Brunauer–Emmett–Teller (BET)[53] and the Barrett–Joyner–Halenda (BJH)[54] models, respectively.

The crystallinity and chemical composition of the sorbents were investigated using powder X-ray diffraction (XRD, Bruker AXS D8 Advance). The X-ray diffractometer was equipped with a Lynxeye super speed detector using Cu Kα radiation (λ = 1.5418 Å, 40 mA and 40 kV). Each sample was measured in the 2θ range of 10–90 ° using a step size of 0.025° with a time duration per step of 0.8 s.

The morphology and textural features of the calcined sorbents were analyzed by high-resolution scanning electron microscopy (HR-SEM) (FEI Magellan 400 FEG) and focused ion beam scanning electron microscopy (FIB-SEM) (Zeiss, FIB-SEM NVision 40). Prior to imaging, the samples were sputter-coated (MED 010) with an approximately 5-nm-thick layer of platinum to improve their conductivity.

2.6. Cyclic CO_2 capture test. The CO_2 uptake of the sorbents was determined over multiple carbonation and calcination cycles in a thermogravimetric analyzer (TGA, Mettler Toledo TGA/DSC 1). In a typical experiment, approximately 5 mg of the calcined sorbent was loaded in an alumina crucible (70 µl) and heated to 900 °C (50 °C/min heating rate) in an overall flow rate of 150 ml/min of N_2 (including a constant purge flow of N_2 , 25 ml/min, over the microbalance). After reaching the reaction temperature, the temperature was maintained for 4 min to completely calcine the material. Subsequently, the temperature was decreased to 650 °C (50 °C/min cooling rate) and the carbonation reaction was performed for 20 min in an atmosphere containing 20 vol. % of CO_2 (30 ml/min) balanced by N_2. Subsequently, the temperature was increased to 900 °C (50 °C/min heating rate) in a flow of 30 ml/min of CO_2 (25 ml/min purge flow of N_2 over the microbalance) to regenerate the sorbent for 10 min. The cyclic carbonation and calcination reactions were repeated 30 times for each sorbent.

2.7. Estimation of the CO_2 uptake in the kinetically controlled reaction stage. The CO_2 uptake in the kinetically controlled reaction stage was estimated following a simple model that assumes that the CO_2 uptake in the kinetically controlled reaction stage has ceased once the pore volume in $d_{pore} < 100$ nm has been filled by $CaCO_3$.[39, 55]:

$$CO_2 \text{ uptake } [g_{CO_2}/g_{CaO}] = \frac{\text{Pore volume (dp < 100 nm)} \times \text{CaO density}}{\text{molar volume ratio (CaCO}_3\text{ to CaO) - 1}} \times \frac{\text{Molecular weight of CO}_2}{\text{Molecular weight of CaO}}$$

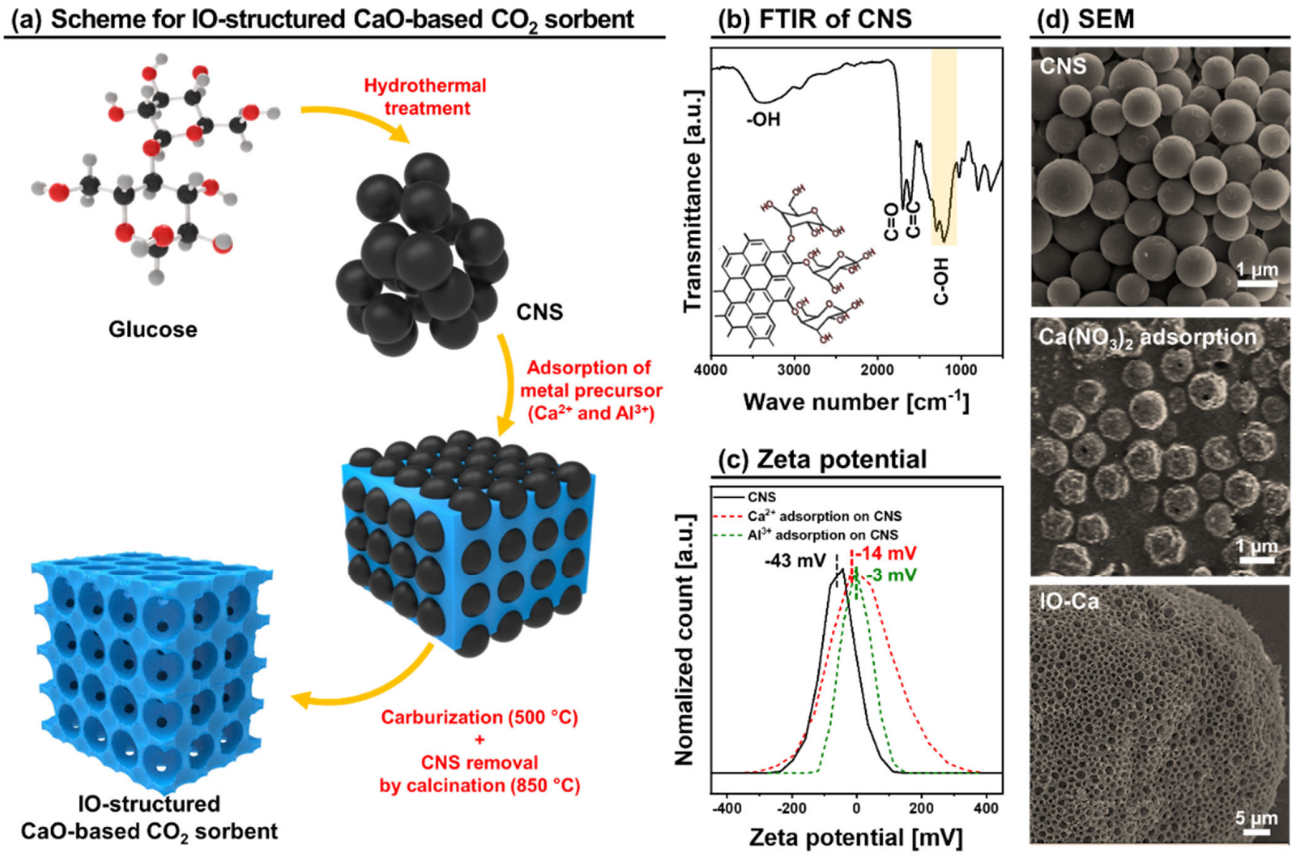

Figure 1. (a) Schematic diagram illustrating the preparation of the IO-like, CaO-based CO_2 sorbent. (b) FTIR of the CNS templates prepared by hydrothermal treatment of an aqueous glucose solution (2.2 M) (c) Zeta potential of CNS before and after immersion into a calcium nitrate solution. The inset in Figure 1b represents the functional groups on the surface of the CNS.(d) SEM images of the CNS template, CNS after $Ca(NO_3)_2{\cdot}4H_2O$ adsorption and calcined IO-Ca_900 nm. The SEM image of carburized IO-Ca_900 nm is given in Figure S1.

3. RESULTS AND DISCUSSION

3.1. Material synthesis. Figure 1 describes the procedure for the preparation of the IO-like, CaO-based CO_2 sorbents using monodispersed carbon nanospheres (CNS). The CNS templates were prepared by the hydrothermal treatment of an aqueous solution of glucose at 180 °C in a Parr bomb (Figure 1a). IR spectroscopy (Figure 1b) reveals bands at 1700 cm^{-1} and 1620 cm^{-1} that can be attributed to C=O stretching and C=C stretching vibrations, respectively, suggesting the aromatization of glucose during the hydrothermal treatment[56]. The bands in the range of 1000–1300 cm^{-1} can be assigned to C–OH stretching and OH bending vibrations, possibly due to carboxylic groups at the surface of the carbon spheres. Such surface functionalities are beneficial for the sorption of metal ions. The CNS have a negative surface charge, i.e., a zeta potential of -43.2 mV in deionized water (Figure 1c). Owing to the negatively charged surface of the CNS, cations (Ca^{2+} and Al^{3+}) in the metal precursor solutions are electrostatically adsorbed on the surface of the CNS. The immersion of CNS into a solution of calcium nitrate and aluminium nitrate solutions leads to an increase in the zeta potential of the CNS from -43.2 to -14.2 mV and to -3.3 mV, respectively, indicating the adsorption of cations, i.e., Ca^{2+} and Al^{3+}, on the surface of the CNS. The final IO structure (Figure 1d) is obtained after drying and carburization at 500 °C in N_2 (0.4 L/min) and the subsequent removal of the CNS by calcination at 900 °C in static air. For IO-Ca_900 nm, a three-dimensional network of large pores (≈ 900 nm) is observed in the calcined material.

3.2. Structural and morphological characterization of the sorbents. The crystallinity and chemical composition of the IO-like structures at different synthesis steps were assessed by XRD. The broad peak located between 2θ = 17–40 ° in the diffractogram of the dried material (Figure 2a) is characteristic for colloidal (amorphous) carbon spheres.[57-60]. The dried material did not show any further reflections, indicative of an amorphous structure of deposited metal precursors. After carburization in N_2 at 500 °C, a calcite phase ($CaCO_3$) was observed. A likely explanation for the formation of $CaCO_3$ is the reaction of the carbonaceous gases produced by the thermal decomposition of the organic species in the CNS template during carbonization with the deposited calcium species. $CaCO_3$ was transformed into lime (CaO) after calcination at 900 °C. Due to the hygroscopic nature of CaO, portlandite ($Ca(OH)_2$), was also observed. For the case that the CNS were immersed in an aqueous solution containing both Al^{3+} and Ca^{2+} cations, tricalcium aluminate ($Ca_3Al_2O_6$) was observed after calcination. The intensity of the $Ca_3Al_2O_6$ peaks increased with increasing Al content (Figure 2b). The diffractogram of calcined IO-Ca_6Al_4_900 contains only reflections due to $Ca_3Al_2O_6$. The quantity of $Ca_3Al_2O_6$ in the sorbents, as determined by Rietveld analysis (Figure 2c and Figure S2), increased from 9.7 wt. % to 100 wt. % for an Al content of, respectively, 5 mol % and 40 mol %. These values are in good agreement with the stoichiometry of $Ca_3Al_2O_6$, indicating that Al is present only in a $Ca_3Al_2O_6$ phase.

The structure of the CNS template and the IO-like CO_2 sorbents (calcined at 900 °C and with different ratios of Ca^{2+} : Al^{3+}) was imaged by SEM. The size of the carbon spheres prepared by the hydrothermal treatment of an aqueous solution of glucose increases with increasing concentration of glucose. Specifically, sphere diameters of 322 ± 21 nm, 611 ± 42 nm and 914 ± 56 nm were determined for glucose concentrations of 0.6 M, 1.1 M, and 2.2 M, respectively (Figure 3a). A higher-resolution image of the IO-like, CaO-based structures reveals a porous, nanostructured backbone (Figure 3b). The presence of interparticle pores, i.e., small pores (d_{pore} < 100 nm) in the CaO backbone can be ascribed to the release of CO_2 during calcination, as $CaCO_3$ decomposes to CaO. On the other hand, the direct calcination of the material without a prior carburization step resulted in the collapse of the structure (Figure S3b), indicating

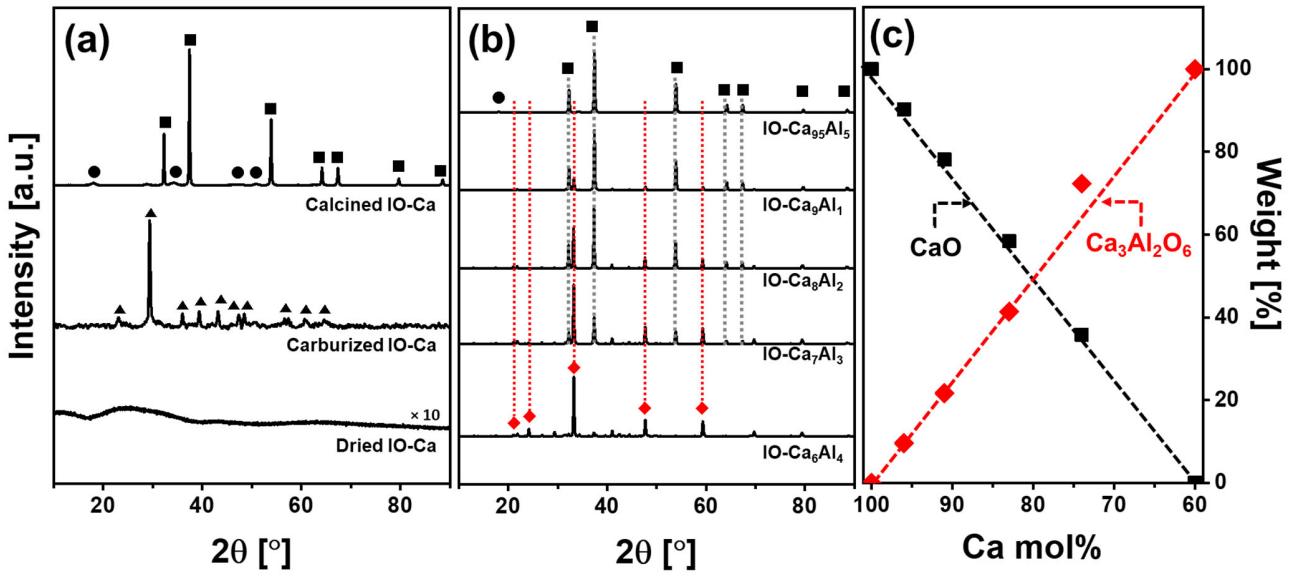

Figure 2. XRD diffractograms of (a) IO-like CaO at different steps of the synthesis, (b) IO-like CaO with different ratios of Ca^{2+} : Al^{3+} (IO-Ca_xAl_y_900 nm), and (c) the weight fractions of CaO and $Ca_3Al_2O_6$ as determined by Rietveld analysis. The dashed lines in Figure 3c give the theoretically expected quantities of CaO and $Ca_3Al_2O_6$ in the materials. The symbols denote (▲) calcite ($CaCO_3$), (■) lime (CaO), (●) portlandite ($Ca(OH)_2$), and (◆) tricalcium aluminate ($Ca_3Al_2O_6$).

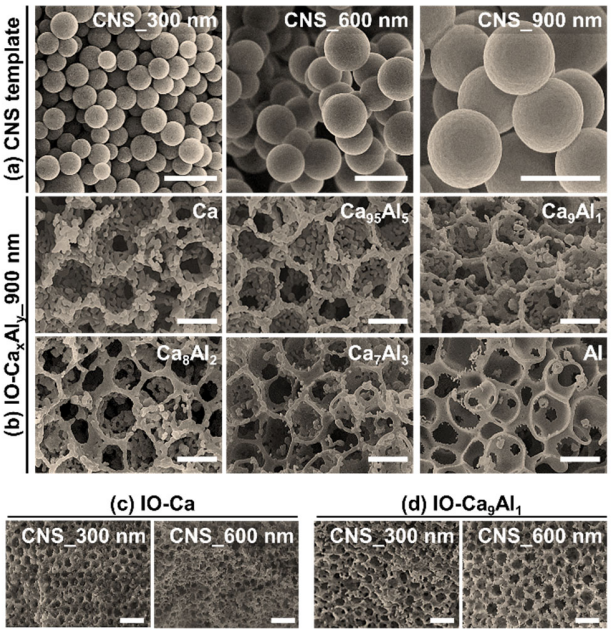

Figure 3. SEM images of (a) CNS templates prepared by the hydrothermal treatment of aqueous glucose solutions (0.6 M, 1.1 M and 2.2 M), corresponding to CNS_300 nm, CNS_600 nm and CNS_900 nm, respectively, (b) freshly calcined IO-Ca$_x$Al$_y$_900 nm with different ratios of Ca^{2+}:Al^{3+} (10:0–5:5), and freshly calcined (c) IO-Ca and (d) IO-Ca$_9$Al$_1$ using different sizes of the CNS template (CNS_300 nm and CNS_600 nm). Scale bar = 1 µm.

that a prior carburization step is essential for obtaining an IO-like structure.

Independent of the ratio of Ca^{2+} to Al^{3+} and the diameter of the carbon sphere template, an IO-like structure could be obtained following the removal of the sacrificial template (Figure 3b-d). The average size of the central, large pores of the IO-like structures are 285 ± 20 nm, 592 ± 27 nm, and 912 ± 28 nm, which is in good agreement with the size of the CNS templates of 300 nm, 600 nm, and 900 nm, respectively. Concerning the homogeneity of the mixture between Al and Ca, SEM/EDX mapping of IO-Ca$_9$Al$_1$_900 nm confirms a rather homogeneous distribution of Al in the CaO matrix (Figure S3d-g).

The pore size distribution of the small pores (d_{pore} < 100 nm) in the backbone of the IO-like structures was determined by N_2 physisorption (Figure S4a and S4b). The N_2 isotherm of the calcined materials is typically of type III with an H3 hysteresis loop (0.1–0.9 of p/p^0), indicative of the presence of both meso- and macropores with a fairly broad pore size distribution. The BJH pore size distribution of the calcined materials (Figure S4c and S4d) shows a bimodal pore size distribution (d_{pore} ≈ 2 nm and 30 nm). Table 1 summarizes the textural properties of the synthetic sorbents and the limestone-derived benchmark sorbent. The textural properties of the IO-like structured materials are superior to those of limestone. For example, IO-Ca_900 nm (i.e., an Al-free material) has a surface area and pore volume of, respectively, 24 $m^2/g_{sorbent}$ and 0.18 $cm^3/g_{sorbent}$, compared to 11 $m^2/g_{sorbent}$ and 0.11 $cm^3/g_{sorbent}$ for freshly calcined limestone. The use of a smaller size for the CNS template slightly enhances the textural properties of the material, e.g., a surface area and pore volume of, respectively, 27 $m^2/g_{sorbent}$ and 0.18 $cm^3/g_{sorbent}$ are obtained for IO-Ca_600 nm and 28 $m^2/g_{sorbent}$ and 0.20 $cm^3/g_{sorbent}$ for IO-Ca_300 nm. Similar observations are made for materials that contain Al, i.e. an increasing surface area and pore volume with a decreasing size of the CNS template. For example, a surface area and pore volume of 43 $m^2/g_{sorbent}$ and 0.25 $cm^3/g_{sorbent}$ were determined for IO-Ca$_9$Al$_1$_300 nm, compared to 31 $m^2/g_{sorbent}$ and 0.22 $cm^3/g_{sorbent}$ for IO-Ca$_9$Al$_1$_900 nm. In particular, the addition of Al_2O_3 to CaO further improves the textural properties of the materials. This is probably due to an increase in the fraction of $Ca_3Al_2O_6$, as the single-phase IO-Ca$_6$Al$_4$_900 nm (i.e., pure $Ca_3Al_2O_6$) exhibits a high surface area (61 $m^2/g_{sorbent}$) and pore volume (0.30 $cm^3/g_{sorbent}$).

Table 1. Textural properties of calcined, IO-structured CaO-based materials and limestone.

Sorbent	ICP-OES[b]	N$_2$ physisorption[c]		
	Ca^{2+}:Al^{3+}	S_{BET} [m^2/g]	$V_{Pore, BJH}$ [cm^3/g]	D_{pore} [nm]
Influence of the molar ratio of Ca^{2+} to Al^{3+} (using CNS-900 nm as template)				
IO-Ca		24	0.18	3.2
IO-Ca$_{95}$Al$_5$	96 : 4	28	0.20	3.1
IO-Ca$_9$Al$_1$	91 : 9	31	0.22	3.3
IO-Ca$_8$Al$_2$	83 : 17	37	0.22	3.2
IO-Ca$_7$Al$_3$	74 : 26	43	0.26	3.6
IO-Ca$_6$Al$_4$	59 : 41	61	0.30	3.3
IO-Al		87	0.33	3.3
Influence of the CNS particle size				
IO-Ca_300 nm		28	0.20	3.1
IO-Ca_600 nm		27	0.18	3.2
IO-Ca_900 nm		24	0.18	3.2
Limestone-derived benchmark[a]		11	0.16	10.7

a: calcined Rheinkalk limestone at 900 °C, b: molar ratio of Ca^{2+} to Al^{3+} determined by ICP-OES, and c: specific surface area (S_{BET}) and pore volume ($V_{Pore, BJH}$) calculated by BET and BJH models, respectively.

3.3. CO_2 capture performance of the sorbents. Cyclic CO_2 capture and regeneration studies were performed in a TGA using practically relevant regeneration conditions (i.e., calcination at 900 °C in a pure CO_2 atmosphere. The temperature programmed calcination of $CaCO_3$ using a mixture of 30 ml/min of CO_2 and 25 ml/min and a N_2 purge flow gave a maxima of the weigh change at 904 °C (Figure S5a), corresponding to an equilibrium partial pressure of CO_2 at the sample of 1.04 bar (Figure S5b; start of $CaCO_3$ decomposition at 876 °C). This suggests that the calcination atmosphere is affected negligibly by the N_2 flow over the micro balance. Figure 4a plots the CO_2 uptake as a function of cycle number for IO-like structures (CNS = 900 nm) and compares them to that of the limestone-derived benchmark. The limestone-derived benchmark exhibits a very high CO_2 uptake of 0.58 $g_{CO2}/g_{sorbent}$ in the 1st cycle. This value decreased rapidly to 0.13 $g_{CO2}/g_{sorbent}$ after 10 cycles of carbonation and calcination. The rapid decay of the CO_2 uptake of limestone (an average decay of 7.7 % per cycle) has been attributed to the loss of the pore volume in pores with a diameter of < 100 nm due to the absence of a structural stabilizer in limestone.[26, 61] Unstabilized IO-like CaO showed a slightly lower decay rate (7.4 % per cycle) than limestone, albeit its deactivation behaviour was very similar. Hence, unstabilized CaO, independent of its initial

structure, is prone to thermal sintering, which translates into a rapidly decreasing CO_2 uptake.

IO-like structures stabilized by $Ca_3Al_2O_6$ improved the cyclic stability of the materials. For a very small fraction of Al, i.e., IO-$Ca_{95}Al_5$_900 nm, we could still observe a gradual decrease in the cyclic CO_2 uptake of the material (i.e., a decay of 3.4 % per cycle), albeit significantly smaller when compared to pure CaO. Increasing the Al content further, i.e., IO-Ca_9Al_1_900 nm, yielded an almost stable CO_2 uptake-regeneration behavior with an average decay rate of only 0.2 % per cycle. Figure 4b plots the CO_2 uptake of IO-Ca_xAl_y_900 nm at the 10th cycle as a function of the Al content. Increasing the Al content beyond 40 mol % resulted in materials with a negligible CO_2 uptake, indicating, as expected, that $Ca_3Al_2O_6$ is inactive for CO_2 capture under the conditions studied here. Within the Ca^{2+}: Al^{3+} range of 70:30 to 90:10, a linear relationship between the CO_2 uptake capacity and the molar fraction of Ca^{2+} was observed.

Using a percolation model and assuming small (< 1 µm) and spherical particles[62] the minimal fraction of $Ca_3Al_2O_6$ to stabilize CaO against sintering is determined as 14 vol. %. The inset in Figure 4b plots the volume percentage of $Ca_3Al_2O_6$ as a function of the mol % of Al in the material. For example, IO-Ca_9Al_1_900 nm contains 23 vol % $Ca_3Al_2O_6$ and exceeds the percolation threshold, whereas the content of $Ca_3Al_2O_6$ in IO-$Ca_{95}Al_5$_900 nm (10 vol. %) is below the percolation threshold. Hence, from a percolation theory point of view IO-$Ca_{95}Al_5$_900 nm is expected to deactivate, which is confirmed by our experimental results. However, the reduction of the CO_2 uptake with high Al loadings suggests that there is a trade-off between the cyclic stability of a material (improving with increasing Al content) and the availability of CO_2-capture-active CaO (increasing with decreasing Al content). The best compromise between these two requirements seems to be an Al content of 10 mol %, i.e., IO-Ca_9Al_1_900 nm which exceeded the CO_2 uptake of limestone after 10 cycles by 340 %.

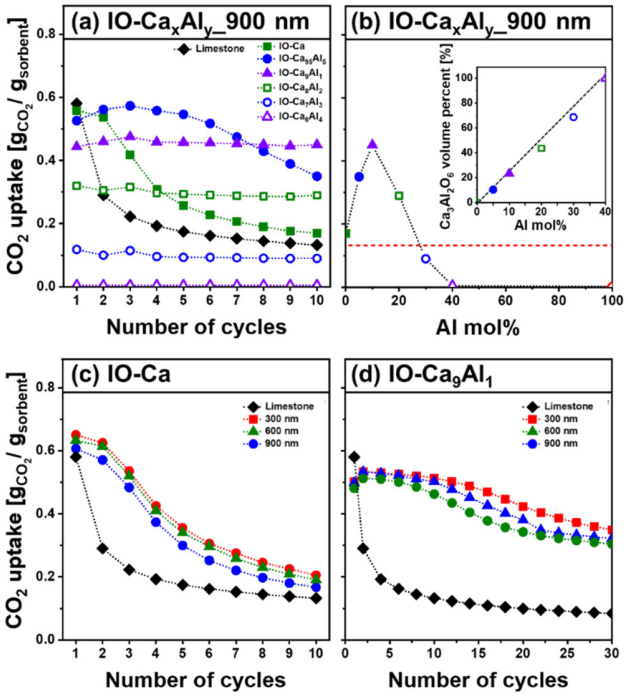

Figure 4. (a) Cyclic CO_2 uptake of IO-like structures using 900 nm CNS and different ratios of Ca^{2+} : Al^{3+}, and (b) CO_2 uptake in the 10th cycle as a function of the molar ratio of Ca : Al. The inset in Figure 4b represents the volume percentage of $Ca_3Al_2O_6$ as a function of the molar ratio of Al. Cyclic CO_2 capture of (c) IO-Ca and (d) IO-Ca_9Al_1 as a function of the size of the CNS template (300–900 nm). The solid horizontal line gives the maximum theoretical CO_2 uptake of pure CaO, i.e., 0.78 $g_{CO_2}/g_{sorbent}$.

Next, we assessed the effect of the size of the CNS template on the cyclic CO_2 uptake of the sorbent. For unstabilized CaO, i.e., IO-Ca (Figure 4c), the CO_2 uptake in the 1st cycle increases only marginally from 0.62 $g_{CO_2}/g_{sorbent}$ to 0.66 $g_{CO_2}/g_{sorbent}$ when the size of the CNS was reduced from 900 to 300 nm. Independent of the size of the CNS template, the materials rapidly deactivated with an average decay rate of 6.9–7.1 % per cycle. The fact that the sizes of the CNS template did not affect appreciably the CO_2 uptake suggests that the average size of the large pores, i.e., pores with d_{pore} of 300–900 nm is not linked critically to the CO_2 uptake. Similarly, we could not observe a significant effect of the size of the CNS template on the CO_2 capture performance for $Ca_3Al_2O_6$-stabilized CaO (Figure 4d). However, it is noteworthy that IO-Ca_9Al_1 exhibited an average capacity decay of only 0.6 % per cycle over the 30 cycles tested,

For limestone-derived CaO, IO-Ca_9Al_1_900 nm and IO-Ca_8Al_2_900 nm, we have extended the number of CO_2 capture and regeneration cycles to 60 (Figure S6). The CO_2 uptake of IO-Ca_9Al_1_900 nm and IO-Ca_8Al_2_900 nm continuously decreased after 10 cycle and 30 cycles, respectively. IO-Ca_8Al_2_900 nm showed an appreciable cyclic stability preserving 84.5 % of its initial CO_2 uptake, outperforming limestone-derived CaO (7 %) and IO-Ca_9Al_1_900 nm (58.7 %). Nevertheless, we observed a comparable CO_2 uptake of IO-Ca_9Al_1_900 nm (0.31 $g_{CO2}/g_{sorbent}$) and IO-Ca_8Al_2_900 nm (0.30 $g_{CO2}/g_{sorbent}$) after the 60th cycle-, surpassing the value of limestone-derived CaO by ~ 780 %.These results indicate that $Ca_3Al_2O_6$ is an effective stabilizer when compared to the unstabilized material.

3.4. Alternative strategy to incorporate a stabilizer into the CaO matrix: Atomic layer deposition. Figure 4b has demonstrated that the incorporation of a $Ca_3Al_2O_6$ stabilizer into the matrix of the sorbent increases the cyclic CO_2 uptake stability of the sorbent; yet, an effective stabilization could only be observed for a stabilizer content exceeding 21 wt. % $Ca_3Al_2O_6$. In an attempt to reduce the quantity of the CO_2-capture-inative stabilizer in the sorbent an alternative technique, i.e., atomic layer deposition (ALD) was utilized. An additional reference material (Ca^{2+} : Al^{3+} = 9:1) was obtained by impregnating IO-Ca_900 nm with an aqueous solution of aluminium nitrate. The resulting materials are denoted as ALD-IO-Ca_9Al_1_900 nm and IMP-IO-Ca_9Al_1_900 nm, respectively. The diffractogram of as-synthesized ALD-IO-Ca_9Al_1_900 nm (i.e directly after ALD coating) revealed the presence of CaO and $Ca(OH)_2$ (Figure S7a); yet, no Al-containing phases such as Al_2O_3 or mixed oxides of calcium and aluminum were observed (Figure S7a), indicating an amorphous nature of the as-grown Al_2O_3 overcoat. On the other hand, we observe the presence of $Ca(OH)_2$ and $Al(NO_3)_3{\cdot}9H_2O$ in dried IMP_IO_Ca_9Al_1_900 nm (Figure S7a). After calcination at 900 °C signatures due to CaO, $Ca_3Al_2O_6$ and $Ca(OH)_2$ are observed in the diffractogram of

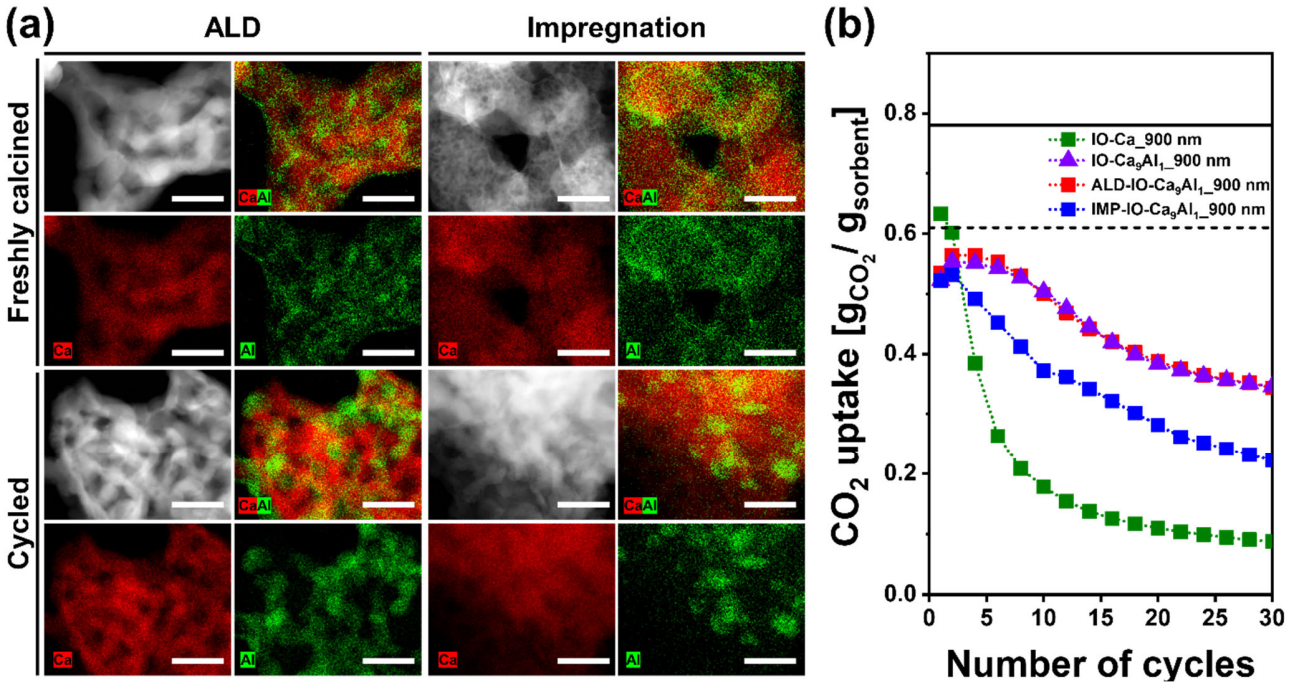

Figure 5. (a) HAADF STEM images with elemental analysis of ALD-IO-Ca_9Al_1_900 nm and IMP-IO-Ca_9Al_1_900 nm (freshly calcined and 30 cycles). Scale bar = 200 nm. (b) Cyclic CO_2 uptake of ALD-IO-Ca_900 nm and IMP-IO-Ca-900 nm. The solid and dashed lines give the maximum theoretical CO_2 uptake of pure CaO, i.e., 0.78 $g_{CO_2}/g_{sorbent}$, and the maximum theoretical CO_2 uptake of the sorbent assuming the full conversion of the CaO in the $Ca_3Al_2O_6$-stabilized sorbent.

IMP_IO_Ca_9Al_1_900 nm and ALD-IO-Ca_9Al_1_900 nm. Quantification by Rietveld analysis reveals a molar ratio Ca^{2+}:Al^{3+} = 9:1 in both ALD-IO-Ca_9Al_1_900 nm and IMP-IO-Ca_9Al_1_900 nm (Figure S7b), indicating that all of the Al_2O_3 formed a crystalline mixed oxide with the CaO matrix.

Unlike IMP-IO-Ca_9Al_1_900 nm which exhibits a partially collapsed IO-like structure, ALD-IO-Ca_9Al_1_900 nm preserved the original structure of IO-Ca_900 nm (Figure 5a and Figure S8). The grain size in ALD-IO-Ca_9Al_1_900 nm (107 ± 13 nm) is comparable to that of fresh IO-Ca_900 nm (96 ± 7 nm) and IO-Ca_9Al_1_900 nm (102 ± 7 nm), whereas the grains in IMP-IO-Ca_9Al_1_900 nm are roughly two-fold larger (217 ± 15 nm) compared to IO-Ca_900 nm (after calcination at 900 °C). Furthermore, STEM images, combined with elemental EDX analysis, of both ALD-IO-Ca_9Al_1_900 nm and IMP-IO-Ca_9Al_1_900 nm reveal that Al-containing CaO grains comprise the backbone of IO-like structure in the calcined materials. However, the original Al_2O_3 film in ALD-IO-Ca_9Al_1_900 nm has been altered significantly during calcination (Figure 5a), owing to the diffusion and chemical interaction of the ALD-grown Al_2O_3 with CaO forming $Ca_3Al_2O_6$.

Figure 5b plots the cyclic CO_2 uptake of IO-Ca_900 nm, IO-Ca_9Al_1_900 nm, ALD-IO-Ca_9Al_1_900 nm and IO-Ca_9Al_1_900 nm. ALD-IO-Ca_9Al_1_900 nm and IO-Ca_9Al_1_900 nm show a very similar behavior with a capacity retention of, respectively, 64 % and 63 % after 30 cycles, whereas a notable capacity decay is observed for IMP-Ca_9Al_1_900 nm, despite containing a comparable fraction of $Ca_3Al_2O_6$.

The micrographs shown in Figure 5a and S5 reveal that the IO-like structures of both ALD-Ca_9Al_1_900 nm and IMP-IO-Ca_9Al_1_900 nm collapsed during 30 cycle operation. This is in line with the observation that the pore volume reduces with cycle number. Specifically, the initial pore volume of ALD-Ca_9Al_1_900 nm (0.23 $cm^3/g_{sorbent}$) and IMP-IO-Ca_9Al_1_900 nm (0.19 $cm^3/g_{sorbent}$) reduced to, respectively, 0.13 $g_{CO_2}/g_{sorbent}$ and 0.05 $g_{CO_2}/g_{sorbent}$ after 30 cycles (Table S1). Also the pore volume of IO-Ca_9Al_1_900 nm decreased from 0.22 $cm^3/g_{sorbent}$ to 0.12 $cm^3/g_{sorbent}$ over 30 cycles (Table S2, discussed in more detail in the following section). Overall, for the investigated materials here, the change in the pore volume with cycle number follows the same trend as the CO_2 uptake.

3.5. Structure–performance relationship. To probe in more detail the possible link between changes in the texture of a sorbent and the decay of its CO_2 uptake, the temporally resolved carbonation profiles of limestone, IO-Ca_900 nm and IO-Ca_9Al_1_900 nm (1st and 10th cycle) were acquired (Figure 6a). Generally, the carbonation reaction occurs in two reaction stages, i.e., a kinetically controlled reaction stage followed by diffusion-limited reaction stage[25, 63-64]. The kinetically controlled reaction stage is characterized by a rapid CO_2 uptake and proceeds via the filling of small pores with $CaCO_3$. The diffusion-limited reaction stage is appreciably slower owing to the slow diffusion of CO_2 through the $CaCO_3$ product layer. The transition between the two reaction regimes was determined as the intersection of two straight lines that approximate the conversion vs. time behaviour in the two reaction stages. In the 1st cycle, approximately 55–65 % of the CaO available is converted to $CaCO_3$ in the kinetically controlled carbonation stage. Unstabilized CaO, i.e., limestone and IO-Ca_900 nm, could retain only ~ 22 % of their initial CO_2 uptake in the kinetically controlled reaction stage after 10 cycles. For $Ca_3Al_2O_6$-stabi-

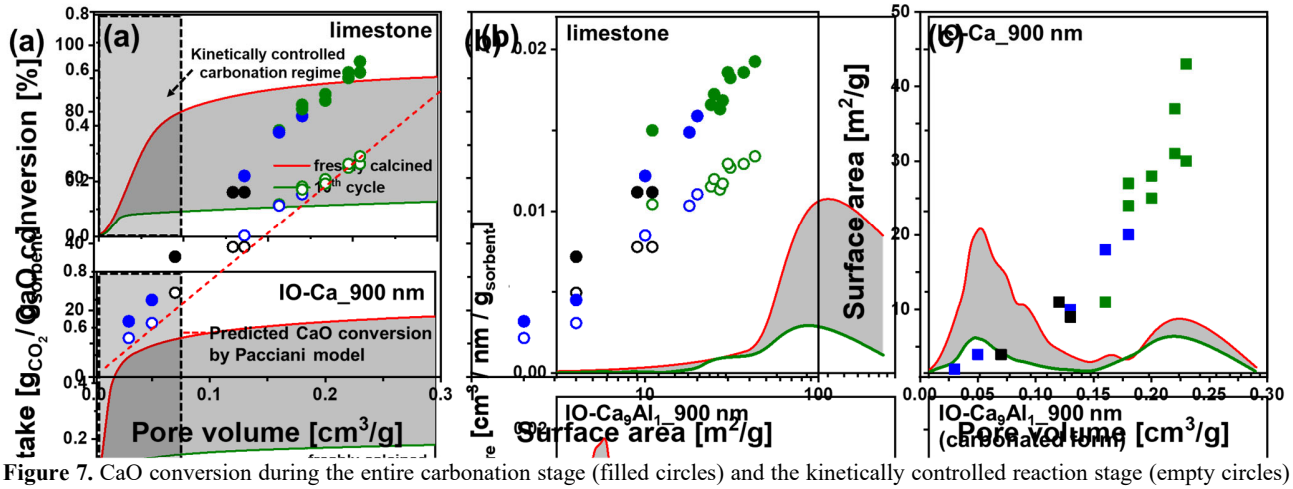

Figure 7. CaO conversion during the entire carbonation stage (filled circles) and the kinetically controlled reaction stage (empty circles) as a function of (a) pore volume, and (b) surface area of the sorbent. (c) Surface area of the freshly calcined and cycled sorbents as a function of pore volume. The color of the square refers to materials that are either freshly calcined (green) or that have undergone 10 (blue) or 30 cycles (black). The dashed line in (a) represents the CaO conversion predicted by the model of Pacciani et al..[39, 55]

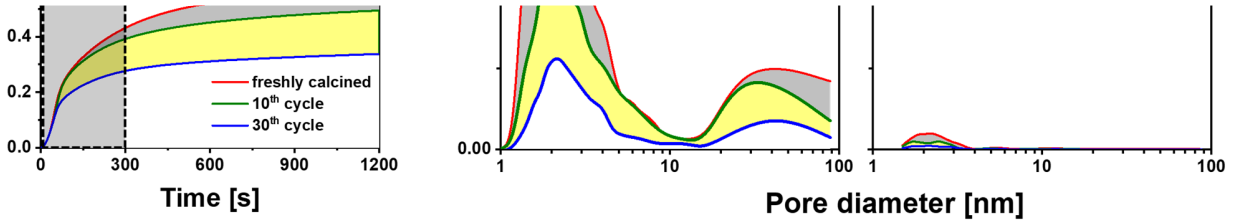

Figure 6. (a) Temporally resolved carbonation profiles of limestone, IO-Ca_900 nm and IO-Ca_9Al_1_900 nm. The reduction in the CO_2 uptake is highlighted by the grey and yellow fill. The reduction in the CO_2 uptake is highlighted by the grey fill. (b) BJH pore size distribution of limestone (calcined form), IO-Ca_900 nm, IO-Ca_9Al_1_900 nm (calcined form), and IO-Ca_9Al_1_900 nm (after 6 min of carbonation). The red, green and blue dashed lines refer to sorbents that have undergone 1, 10, and 30 cycles, respectively. The reduction in the CO_2 uptake is highlighted by the grey and yellow fill.

lized CaO, i.e., IO-Ca_9Al_1_900 nm, 95 % of the initial CO_2 uptake in the kinetically controlled carbonation stage was retained after 10 cycles; yet this value decreased further upon increasing the cycle number, yielding 65 % retention after 30 cycles. Similarly, high retention values are obtained for the other two Al_2O_3 containing sorbents of ALD-IO-Ca_9Al_1_900 nm and IMP-IO-Ca_9Al_1_900 nm. The retention of the CO_2 uptake in the kinetically controlled stage of the carbonation reaction after 30 cycles are 61 % and 42 % for ALD-IO-Ca_9Al_1_900 nm and IMP-IO-Ca_9Al_1_900 nm, respectively (Figure S9).

In order to assess which morphological features dominantly control the CO_2 uptake in the kinetically controlled carbonation stage, the BJH pore size distribution was determined as a function of cycle number. We observe a dramatic decrease in the pore volume (with $d_{pore} < 100$ nm) with cycle number for unstabilized CaO, i.e., limestone and IO-Ca_900 nm (Figure 6b). After 10 cycles, the initial pore volume of limestone and IO-Ca_900 nm (0.11 $cm^3/g_{sorbent}$ and 0.18 $cm^3/g_{sorbent}$, respectively) decreased to 0.03 $g_{CO_2}/g_{sorbent}$ and 0.05 $g_{CO_2}/g_{sorbent}$, respectively (Table S1). On the other hand, for $Ca_3Al_2O_6$-stabilized CaO, i.e., IO-Ca_9Al_1_900 nm, a pore volume of 0.17 $cm^3/g_{sorbent}$ is retained in pores with $d_{pore} < 100$ nm after 10 cycles. However, the pore volume in IO-Ca_9Al_1_900 nm decreased to 0.10 $cm^3/g_{sorbent}$ after 30 cycles (Figure 6b), which is, however, substantially higher than that of the unstabilized sorbents. Overall, the reduction in pore volume shows a very similar trend as the decay of the CO_2 capture capacity of the sorbents.

To probe the hypothesis that the CO_2 uptake in the kinetically controlled reaction stage is controlled by the availability of pore volume in pores with a diameter $d_{pore} < 100$ nm,[39, 55] we recorded the temporally resolved CO_2 uptake and changes in the pore volume of the materials with cycle number. Independent of the sorbent, we observe that at a certain point in the reaction the rate of CO_2 capture reduced significantly, indicative of the transition of the carbonation reaction from the kinetically controlled to the diffusion-limited stage (Figure S10). We also observed, that for IO-Ca_9Al_1_900 nm the pore volume in pores with $d_{pore} < 100$ nm is negligible after 6 min of carbonation (Figure 6b). Taking the measured surface area (as determined by the BET model[53]) and the CO_2 uptake at the end of kinetically controlled carbonation regime (Table S1), the product layer thickness in IO-Ca_9Al_1_900 nm was estimated to be 30 nm, 45 and 54 nm after 1, 10 and 30 cycles, respectively. These values are in good agreement with the previously estimated critical product layer thickness (i.e., the product layer thickness when the kinetically-controlled carbonation becomes diffusion limited) of 50 nm.[63] Hence, our data support the hypothesis that the kinetically controlled carbonation stage ceases once pores with $d_{pore} < 100$ nm have been filled with $CaCO_3$. This observation holds for all of the sorbents (also at different cycle numbers) investigated here.

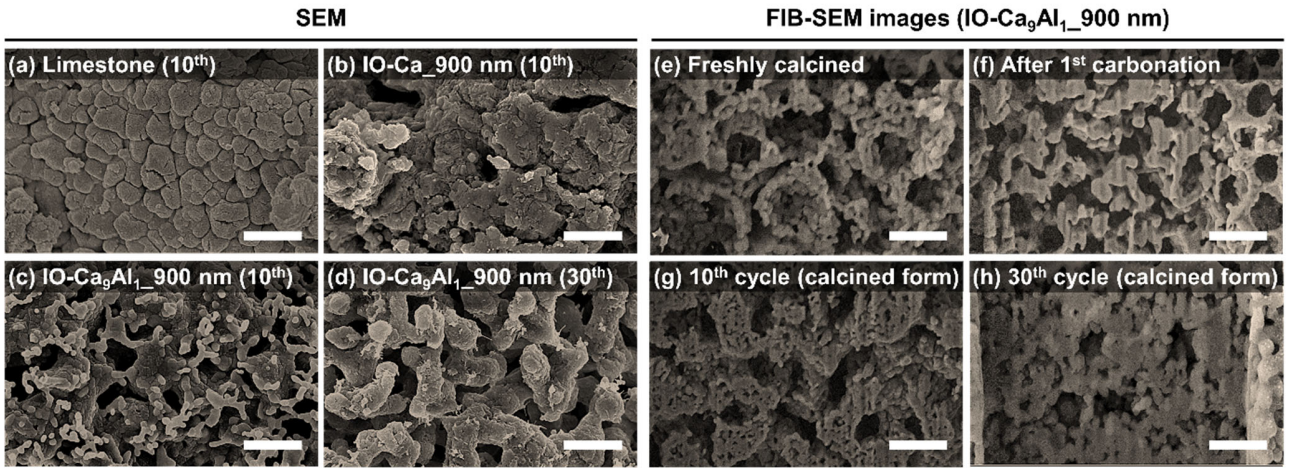

Figure 8. SEM images of (a) limestone, (b) IO-Ca_900 nm and (c and d) IO-Ca_9Al_1 after repeated carbonation and calcination cycles (calcined form). SEM images showing the FIB-enabled cross-sections of (e) freshly calcined, (f) carbonated and reacted (calcined form), after (g) 10 and (h) 30 cycles. Scale bar = 1 µm.

To predict the CO_2 uptake of CaO-based sorbents in the kinetically controlled carbonation regime, Pacciani et al. proposed a simple model assuming that the CO_2 uptake is exclusively controlled by the availability of small pores with $d_{pore} < 100$ nm.[39, 55] Figure 7a shows that there is indeed a linear relationship between the CO_2 uptake in the kinetically controlled carbonation stage and the pore volume in pores with $d_{pore} < 100$ nm. Figure 7b plots the conversion of CaO as a function of the surface area of the sorbent in the calcined state. Both the total conversion of CaO and the CaO conversion in the kinetically controlled reaction stage show a linear relationship with the surface area of the sorbent. This implies that not only the CO_2 uptake in the kinetically controlled but also in the diffusion-limited reaction stage are controlled by the surface area of the sorbent. It is clear that the CO_2 uptake in the diffusion-limited reaction stage should scale linearly with the surface area, whereas the linear relationship between the surface area and the CO_2 uptake in the kinetically controlled reaction stage is most likely due to the direct relationship between pore volume and surface area. These findings confirm that the CaO conversion can be maximized by optimizing the textural properties, i.e., surface area and pore volume, of the sorbent and stabilizing such structures effectively against sintering.

The extent of sintering for the cycled sorbents was assessed further by measuring the size of the grains by electron microscopy. The size of the backbone-comprising grains increased 2.5-fold (525 ± 38 nm) and 3.2-fold (307 ± 23 nm) for, respectively, limestone and IO-Ca_900 nm over 10 cycles (Figure 8a and Figure 8b). On the other hand, the size of the grains in IO-Ca_9Al_1_900 nm grew only marginally from 102 ± 7 to 125 ± 17 nm over 10 cycles (Figure 8c), with a further increase to 241 ± 15 nm after 30 cycles (Figure 8d). Yet, this grain size is still appreciably smaller than in the unstabilized sorbents after 10 cycles.

To visualize the change in the morphology of the sorbents over repeated carbonation and calcination cycles, FIB-cross-sections of IO-Ca_9Al_1_900 nm were scrutinized (Figure 8e-h). In a freshly calcined material, the IO-like structure contains a large number of small pores in the CaO backbone. After the 1st carbonation step of IO-Ca_9Al_1_900 nm, small pores ($d_{pore} < 100$ nm) in the backbone of the IO-like structure were not visible anymore (Figure 8f), which is in line with a negligible pore volume after carbonation (Figure 6b and Table S2). The decrease of the size of the large pores from 820 ± 42 nm to 605 ± 35 nm is mainly related to the volumetric expansion of the material upon carbonation. After 10 cycles (calcined state), the size of the large pores decreased further to 520 ± 50 nm and the grain size in the CaO backbone increased to 270 ± 30 nm, indicative of sintering (Figure 8g). However, our results indicate that large pores play only a minor role in the CO_2 uptake performance of the sorbent investigated here. The inverse opal structure underwent a collapse after 30 cycles (Figure 8h). These findings, in combination with the CaO conversion measurements in the kinetically controlled carbonation stage suggest that the decay of the CO_2 uptake is largely ascribed to the sintering-induced alteration of the textural properties in pores with $d_{pore} < 100$ nm.

4. CONCLUSIONS

To summarize, we have synthesized inverse opal (IO)-like, CaO-based CO_2 sorbents stabilized by $Ca_3Al_2O_6$ that has been introduced via different routes, i.e., one-pot synthesis, impregnation and ALD. The best sorbents synthesized (one-pot synthesis route and an ALD-assisted method) show a high CO_2 uptake over 30 cycles, outperforming the benchmark sorbent derived from limestone and IMP-IO-Ca_9Al_1_900 nm by ~400 % and ~150 %, respectively. We demonstrate that ALD allows for a homogeneous incorporation of the structural stabilizer Al_2O_3 that, upon calcination, reacts with CaO to form $Ca_3Al_2O_6$. The resultant mixed oxide stabilizes the porous structure against sintering and hence, the sorbent largely maintains the pore volume in pores with a diameter $d_{pore} < 100$ nm (preserving 57 % of initial pore volume over 30 cycles). In contrast, the addition of Al_2O_3 via impregnation was not as effective in stabilizing the IO-like structure. We record a reduction in the pore volume by 74 % over 30 cycles. Temporally resolved CO_2 capture profiles combined with a detailed textural characterization reveal that the volume in pores of size $d_{pore} < 100$ nm in the CaO backbone and the total surface area of the sorbent are the primary determinants for the CO_2 uptake in both the kinetically controlled and diffusion-limited carbonation stages.

ASSOCIATED CONTENT

Supporting Information. Textural properties of freshly calcined and cycled sorbents; Rietveld refinement of the diffractograms of calcined sorbent; Scanning electron micrographs with Energy-dispersive X-ray spectroscopy analysis of freshly calcined and cycled sorbent; CO_2 capture rate of the sorbent as a function of carbonation time.

AUTHOR INFORMATION

Corresponding Author

* E-mail address: muelchri@ethz.ch

Notes

The authors declare no competing financial interest.

ACKNOWLEDGMENT

The authors gratefully acknowledge ETH (ETH 57 12-2) and the Swiss National Science Foundation (200020_156015) for financial support. We would like to thank the Scientific Center for Optical and Electron Microscopy (ScopeM) and Center for Micro- and Nanoscience (FIRST) at ETH Zurich for providing training and access to electron microscopes.

REFERENCES

(1) *IPCC, 2014: Climate Change 2014: Synthesis Report*; The Intergovernmental Panel on Climate Change (IPCC): Geneva, 2014.

(2) Levina, E.; Bennett, S.; McCoy, S.; International Energy, A., *Technology roadmap : carbon capture and storage*. IEA: Paris, 2013.

(3) *World Energy Outlook 2015*. IEA: Paris, 2015.

(4) Yu, K. M. K.; Curcic, I.; Gabriel, J.; Tsang, S. C. E., Recent Advances in CO_2 Capture and Utilization. *ChemSusChem* **2008,** *1*, 893-899.

(5) Taylor, P., *Energy Technology Perspectives 2010–Scenarios and Strategies to 2050*. IEA: Paris, 2010.

(6) Aresta, M.; Dibenedetto, A., Utilisation of CO_2 as a chemical feedstock: opportunities and challenges. *Dalton Trans.* **2007**, 2975-2992.

(7) Otto, A.; Grube, T.; Schiebahn, S.; Stolten, D., Closing the loop: captured CO_2 as a feedstock in the chemical industry. *Energy Environ. Sci.* **2015,** *8*, 3283-3297.

(8) Kondratenko, E. V.; Mul, G.; Baltrusaitis, J.; Larrazabal, G. O.; Perez-Ramirez, J., Status and perspectives of CO_2 conversion into fuels and chemicals by catalytic, photocatalytic and electrocatalytic processes. *Energy Environ. Sci.* **2013,** *6*, 3112-3135.

(9) Kim, S. M.; Abdala, P. M.; Margossian, T.; Hosseini, D.; Foppa, L.; Armutlulu, A.; van Beek, W.; Comas-Vives, A.; Copéret, C.; Müller, C., Cooperativity and Dynamics Increase the Performance of NiFe Dry Reforming Catalysts. *J. Am. Chem. Soc.* **2017,** *139*, 1937-1949.

(10) Margossian, T.; Larmier, K.; Kim, S. M.; Krumeich, F.; Fedorov, A.; Chen, P.; Müller, C. R.; Copéret, C., Molecularly Tailored Nickel Precursor and Support Yield a Stable Methane Dry Reforming Catalyst with Superior Metal Utilization. *J. Am. Chem. Soc.* **2017,** *139*, 6919-6927.

(11) Kim, S. M.; Abdala, P. M.; Broda, M.; Hosseini, D.; Copéret, C.; Müller, C., Integrated CO_2 Capture and Conversion as an Efficient Process for Fuels from Greenhouse Gases. *ACS Catal.* **2018,** *8*, 2815-2823.

(12) Tian, S.; Yan, F.; Zhang, Z.; Jiang, J., Calcium-looping reforming of methane realizes in situ CO_2 utilization with improved energy efficiency. *Science Advances* **2019,** *5*, eaav5077.

(13) Bello, A.; Idem, R. O., Pathways for the Formation of Products of the Oxidative Degradation of CO_2-Loaded Concentrated Aqueous Monoethanolamine Solutions during CO_2 Absorption from Flue Gases. *Ind. Eng. Chem. Res.* **2005,** *44*, 945-969.

(14) Goff, G. S.; Rochelle, G. T., Monoethanolamine Degradation: O_2 Mass Transfer Effects under CO_2 Capture Conditions. *Ind. Eng. Chem. Res.* **2004,** *43*, 6400-6408.

(15) Fine, N. A.; Goldman, M. J.; Rochelle, G. T., Nitrosamine Formation in Amine Scrubbing at Desorber Temperatures. *Environ. Sci. Technol.* **2014,** *48*, 8777-8783.

(16) Veltman, K.; Singh, B.; Hertwich, E. G., Human and Environmental Impact Assessment of Postcombustion CO_2 Capture Focusing on Emissions from Amine-Based Scrubbing Solvents to Air. *Environ. Sci. Technol.* **2010,** *44*, 1496-1502.

(17) Duan, Y.; Sorescu, D. C., CO_2 capture properties of alkaline earth metal oxides and hydroxides: a combined density functional theory and lattice phonon dynamics study. *J. Chem. Phys.* **2010,** *133*, 074508.

(18) Hutson, N. D.; Speakman, S. A.; Payzant, E. A., Structural Effects on the High Temperature Adsorption of CO_2 on a Synthetic Hydrotalcite. *Chem. Mater.* **2004,** *16*, 4135-4143.

(19) Wei, J.; Zhou, D.; Sun, Z.; Deng, Y.; Xia, Y.; Zhao, D., A Controllable Synthesis of Rich Nitrogen-Doped Ordered Mesoporous Carbon for CO_2 Capture and Supercapacitors. *Adv. Funct. Mater.* **2013,** *23*, 2322-2328.

(20) Hao, G.-P.; Li, W.-C.; Qian, D.; Lu, A.-H., Rapid Synthesis of Nitrogen-Doped Porous Carbon Monolith for CO_2 Capture. *Adv. Mater.* **2010,** *22*, 853-857.

(21) Yazaydın, A. Ö.; Snurr, R. Q.; Park, T.-H.; Koh, K.; Liu, J.; LeVan, M. D.; Benin, A. I.; Jakubczak, P.; Lanuza, M.; Galloway, D. B.; Low, J. J.; Willis, R. R., Screening of Metal−Organic Frameworks for Carbon Dioxide Capture from Flue Gas Using a Combined Experimental and Modeling Approach. *J. Am. Chem. Soc.* **2009,** *131*, 18198-18199.

(22) Xiang, S.; He, Y.; Zhang, Z.; Wu, H.; Zhou, W.; Krishna, R.; Chen, B., Microporous metal-organic framework with potential for carbon dioxide capture at ambient conditions. *Nat. Commun.* **2012,** *3*, 954.

(23) Ober, J. A. *Mineral commodity summaries 2016*; Reston, VA, 2016; p 205.

(24) Tian, S.; Jiang, J.; Zhang, Z.; Manovic, V., Inherent potential of steelmaking to contribute to decarbonisation targets via industrial carbon capture and storage. *Nat. Commun.* **2018,** *9*, 4422.

(25) Pacciani, R.; Müller, C.; Davidson, J.; Dennis, J.; Hayhurst, A., Synthetic Ca-based solid sorbents suitable for capturing CO_2 in a fluidized bed. *Can. J. Chem. Eng.* **2008,** *86*, 356-366.

(26) Kierzkowska, A. M.; Pacciani, R.; Müller, C. R., CaO-Based CO_2 Sorbents: From Fundamentals to the Development of New, Highly Effective Materials. *ChemSusChem* **2013,** *6*, 1130-1148.

(27) Broda, M.; Müller, C. R., Sol–gel-derived, CaO-based, ZrO_2-stabilized CO_2 sorbents. *Fuel* **2014,** *127*, 94-100.
(28) Broda, M.; Kierzkowska, A. M.; Müller, C. R., Application of the Sol–Gel Technique to Develop Synthetic Calcium-Based Sorbents with Excellent Carbon Dioxide Capture Characteristics. *ChemSusChem* **2012,** *5*, 411-418.
(29) Filitz, R.; Kierzkowska, A. M.; Broda, M.; Müller, C. R., Highly Efficient CO_2 Sorbents: Development of Synthetic, Calcium-Rich Dolomites. *Environ. Sci. Technol.* **2012,** *46*, 559-565.
(30) Lu, H.; Khan, A.; Pratsinis, S. E.; Smirniotis, P. G., Flame-Made Durable Doped-CaO Nanosorbents for CO_2 Capture. *Energy Fuels* **2009,** *23*, 1093-1100.
(31) Broda, M.; Müller, C. R., Synthesis of Highly Efficient, Ca-Based, Al_2O_3-Stabilized, Carbon Gel-Templated CO_2 Sorbents. *Adv. Mater.* **2012,** *24*, 3059-3064.
(32) Armutlulu, A.; Naeem, M. A.; Liu, H.-J.; Kim, S. M.; Kierzkowska, A.; Fedorov, A.; Müller, C. R., Multishelled CaO Microspheres Stabilized by Atomic Layer Deposition of Al_2O_3 for Enhanced CO_2 Capture Performance. *Adv. Mater.* **2017,** *29*, 1702896.
(33) Wang, K.; Clough, P. T.; Zhao, P.; Anthony, E. J., Synthesis of highly effective stabilized CaO sorbents via a sacrificial N-doped carbon nanosheet template. *J. Mater. Chem. A* **2019,** *7*, 9173-9182.
(34) Ma, X.; Li, Y.; Duan, L.; Anthony, E.; Liu, H., CO_2 capture performance of calcium-based synthetic sorbent with hollow core-shell structure under calcium looping conditions. *Appl. Energy* **2018,** *225*, 402-412.
(35) Li, S.; Jiang, T.; Xu, Z.; Zhao, Y.; Ma, X.; Wang, S., The Mn-promoted double-shelled $CaCO_3$ hollow microspheres as high efficient CO_2 adsorbents. *Chem. Eng. J.* **2019,** *372*, 53-64.
(36) Antzara, A. N.; Arregi, A.; Heracleous, E.; Lemonidou, A. A., In-depth evaluation of a ZrO_2 promoted CaO-based CO_2 sorbent in fluidized bed reactor tests. *Chem. Eng. J.* **2018,** *333*, 697-711.
(37) López, J. M.; Grasa, G.; Murillo, R., Evaluation of the effect of inert support on the carbonation reaction of synthetic CaO-based CO_2 sorbents. *Chem. Eng. J.* **2018,** *350*, 559-572.
(38) Alvarez, D.; Abanades, J. C., Determination of the Critical Product Layer Thickness in the Reaction of CaO with CO_2. *Ind. Eng. Chem. Res.* **2005,** *44*, 5608-5615.
(39) Dennis, J. S.; Pacciani, R., The rate and extent of uptake of CO_2 by a synthetic, CaO-containing sorbent. *Chem. Eng. Sci.* **2009,** *64*, 2147-2157.
(40) Liu, W.; Feng, B.; Wu, Y.; Wang, G.; Barry, J.; Diniz da Costa, J. C., Synthesis of Sintering-Resistant Sorbents for CO_2 Capture. *Environ. Sci. Technol.* **2010,** *44*, 3093-3097.
(41) Li, L.; King, D. L.; Nie, Z.; Howard, C., Magnesia-Stabilized Calcium Oxide Absorbents with Improved Durability for High Temperature CO_2 Capture. *Ind. Eng. Chem. Res.* **2009,** *48*, 10604-10613.
(42) Phalak, N.; Deshpande, N.; Fan, L.-S., Investigation of high-temperature steam hydration of naturally derived calcium oxide for improved carbon dioxide capture capacity over multiple cycles. *Energy Fuels* **2012,** *26*, 3903-3909.
(43) Ozcan, D. C.; Shanks, B. H.; Wheelock, T. D., Improving the stability of a CaO-based sorbent for CO_2 by thermal pretreatment. *Ind. Eng. Chem. Res.* **2011,** *50*, 6933-6942.
(44) Koirala, R.; Reddy, G. K.; Smirniotis, P. G., Single nozzle flame-made highly durable metal doped Ca-based sorbents for CO_2 capture at high temperature. *Energy Fuels* **2012,** *26*, 3103-3109.
(45) Kierzkowska, A. M.; Müller, C. R., Sol–Gel-Derived, Calcium-Based, Copper-Functionalised CO_2 Sorbents for an Integrated Chemical Looping Combustion–Calcium Looping CO_2 Capture Process. *ChemPlusChem* **2013,** *78*, 92-100.
(46) Kim, S. M.; Kierzkowska, A. M.; Broda, M.; Müller, C. R., Sol-gel Synthesis of $MgAl_2O_4$-stabilized CaO for CO_2 Capture. *Energy Procedia* **2017,** *114*, 220-229.
(47) Liu, F.-Q.; Li, W.-H.; Liu, B.-C.; Li, R.-X., Synthesis, characterization, and high temperature CO_2 capture of new CaO based hollow sphere sorbents. *J. Mater. Chem. A* **2013,** *1*, 8037-8044.
(48) Kim, S. M.; Liao, W.-C.; Kierzkowska, A. M.; Margossian, T.; Hosseini, D.; Yoon, S.; Broda, M.; Copéret, C.; Müller, C. R., *In Situ* XRD and Dynamic Nuclear Polarization Surface Enhanced NMR Spectroscopy Unravel the Deactivation Mechanism of CaO-Based, $Ca_3Al_2O_6$-Stabilized CO_2 Sorbents. *Chem. Mater.* **2018,** *30*, 1344-1352.
(49) Wang, Y.; Zhang, W.; Li, R.; Duan, W.; Liu, B., Design of stable cage-like CaO/$CaZrO_3$ hollow spheres for CO_2 capture. *Energy Fuels* **2016,** *30*, 1248-1255.
(50) Naeem, M. A.; Armutlulu, A.; Imtiaz, Q.; Donat, F.; Schäublin, R.; Kierzkowska, A.; Müller, C. R., Optimization of the structural characteristics of CaO and its effective stabilization yield high-capacity CO_2 sorbents. *Nat. Commun.* **2018,** *9*, 2408.
(51) Naeem, M. A.; Armutlulu, A.; Broda, M.; Lebedev, D.; Muller, C. R., The development of effective CaO-based CO_2 sorbents via a sacrificial templating technique. *Faraday Discuss.* **2016,** *192*, 85-95.
(52) Sun, X.; Li, Y., Colloidal Carbon Spheres and Their Core/Shell Structures with Noble-Metal Nanoparticles. *Angew. Chem. Int. Ed.* **2004,** *43*, 597-601.
(53) Brunauer, S.; Emmett, P. H.; Teller, E., Adsorption of Gases in Multimolecular Layers. *J. Am. Chem. Soc.* **1938,** *60*, 309-319.
(54) Barrett, E. P.; Joyner, L. G.; Halenda, P. P., The Determination of Pore Volume and Area Distributions in Porous Substances. I. Computations from Nitrogen Isotherms. *J. Am. Chem. Soc.* **1951,** *73*, 373-380.
(55) Pacciani, R.; Müller, C. R.; Davidson, J. F.; Dennis, J. S.; Hayhurst, A. N., Synthetic Ca-based solid sorbents suitable for capturing CO_2 in a fluidized bed. *Can. J. Chem. Eng.* **2008,** *86*, 356-366.
(56) Sakaki, T.; Shibata, M.; Miki, T.; Hirosue, H.; Hayashi, N., Reaction model of cellulose decomposition in near-critical water and fermentation of products. *Bioresour. Technol.* **1996,** *58*, 197-202.
(57) Chen, J.; Duan, L.; Sun, Z., Accurate Control of Cage-Like CaO Hollow Microspheres for Enhanced CO_2 Capture in Calcium Looping via a Template-Assisted Synthesis Approach. *Environ. Sci. Technol.* **2019,** *53*, 2249-2259.
(58) Wang, S.; Shen, H.; Fan, S.; Zhao, Y.; Ma, X.; Gong, J., CaO-based meshed hollow spheres for CO_2 capture. *Chem. Eng. Sci.* **2015,** *135*, 532-539.
(59) Zhu, J.; Li, R.; Niu, W.; Wu, Y.; Gou, X., Facile hydrogen generation using colloidal carbon supported

cobalt to catalyze hydrolysis of sodium borohydride. *J. Power Sources* **2012,** *211*, 33-39.

(60) Lai, X.; Li, J.; Korgel, B. A.; Dong, Z.; Li, Z.; Su, F.; Du, J.; Wang, D., General Synthesis and Gas-Sensing Properties of Multiple-Shell Metal Oxide Hollow Microspheres. *Angew. Chem. Int. Ed.* **2011,** *50*, 2738-2741.

(61) Grasa, G. S.; Abanades, J. C., CO_2 Capture Capacity of CaO in Long Series of Carbonation/Calcination Cycles. *Ind. Eng. Chem. Res.* **2006,** *45*, 8846-8851.

(62) Ewen, P. J. S.; Robertson, J. M., A percolation model of conduction in segregated systems of metallic and insulating materials: application to thick film resistors. *J. Phys. D: Appl. Phys.* **1981,** *14*, 2253.

(63) Barker, R., The reversibility of the reaction $CaCO_3 \rightleftarrows CaO+CO_2$. *J. Appl. Chem. Biotechnol.* **1973,** *23*, 733-742.

(64) Dennis, J.; Pacciani, R., The rate and extent of uptake of CO_2 by a synthetic, CaO-containing sorbent. *Chem. Eng. Sci.* **2009,** *64*, 2147-2157.